Thermoelectric transport of type-I, II, and III massless Dirac fermions in a two-dimensional lattice model

Tomonari Mizoguchi, Hiroyasu Matsuura, and Masao Ogata

Phys. Rev. B **105**, 205203 — Published 16 May 2022

DOI: 10.1103/PhysRevB.105.205203

Thermoelectric transport of type-I, II, and III massless Dirac fermions in two-dimensional lattice model

Tomonari Mizoguchi,[1] Hiroyasu Matsuura,[2] and Masao Ogata[2,3]

[1]*Department of Physics, University of Tsukuba, 1-1-1 Tennodai, Tsukuba, Ibaraki 305-8571, Japan*[*]
[2]*Department of Physics, University of Tokyo, 7-3-1 Hongo, Bunkyo-ku, Tokyo 113-0033, Japan*
[3]*Trans-scale Quantum Science Institute, University of Tokyo, Bunkyo-ku, Tokyo 113-0033, Japan*

(Dated: April 25, 2022)

We study longitudinal electric and thermoelectric transport coefficients of Dirac fermions on a simple lattice model where tuning of a single parameter enables us to change the type of Dirac cones from type-I to type-II. We pay particular attention to the behavior of the critical situation, i.e., the type-III Dirac cone. We find that the transport coefficients of the type-III Dirac fermions behave neither the limiting case of the type-I nor type-II. On one hand, the qualitative behaviors of the type-III case are similar to those of the type-I. On the other hand, the transport coefficients do not change monotonically upon increasing the tilting, namely, the largest thermoelectric response is obtained not for the type-III case but for the optimally tilted type-I case. For the optimal case, the sizable transport coefficients are obtained, e.g., the dimensionless figure of merit being 0.18.

I. INTRODUCTION

In the past few decades, Dirac fermions in solids have attracted considerable interest. In particular, two-dimensional systems hosting Dirac cones have been intensively investigated, both theoretically and experimentally. Graphene, a single-layered honeycomb network of carbon atoms, is a prime example of massless Dirac-fermion systems [1–3]. The organic conductor α-(BEDT-TTF)$_2$I$_3$ [4–10] is another example of the massless Dirac-fermion systems in quasi-two dimensions. An interesting feature of α-(BEDT-TTF)$_2$I$_3$ is that the Dirac cones are not isotropic in the momentum space, i.e., the cones are tilted. Triggered by this finding, the effects of tilting of Dirac cones have been investigated. It was revealed that the Dirac cones are classified into three types according to the degree of tilting: The tilted Dirac cone with the ellipsoidal equi-energy surface around the Dirac point is classified into the type-I. By further increasing the tilting, the Dirac cones are "overtilted" and the equi-energy surface turns into the hyperbola; such a Dirac cone is classified into the type-II. The critical point between the type-I and the type-II is called the type-III Dirac cone, where one of the bands consisting of the Dirac cone has a flat dispersion along a certain direction, resulting in a diverging density of state (DOS) at the Dirac point. Although the type-III Dirac cone is rare compared with the other two types because it does not appear as a stable "phase" occupying a finite region of the parameter space, it has gained attention recently [11–27].

Along with the studies from the viewpoint of electronic structure, exotic transport [7, 9, 28–33] and magnetic properties [34–38] of Dirac fermions have also been studied. The main targets of such studies are the type-I and type-II Dirac cones and thus the properties of the type-III Dirac cones have been less understood compared with the other two types. Since the type-III is the critical point between the type-I and the type-II, one may have the following question: Can we understand the behavior of the type-III Dirac cones by taking the limit from the type-I or type-II?

So far, electric and thermoelectric transports for tilted Dirac fermions, both the longitudinal and transverse ones, have been intensively studied [31, 39–44]. However, previous works are mostly on continuum models, and the study on lattice models is limited. (For instance, for the three-dimensional case, the studies on the minimal lattice model [45] were reported in Refs. [46, 47].) In the continuum model, however, there is a subtlety of the momentum cut-off dependence, namely, for types II and III, the Fermi surface extends far away from the Dirac point, where the Dirac-Hamiltonian description is broken down in actual materials. This hampers the study on the

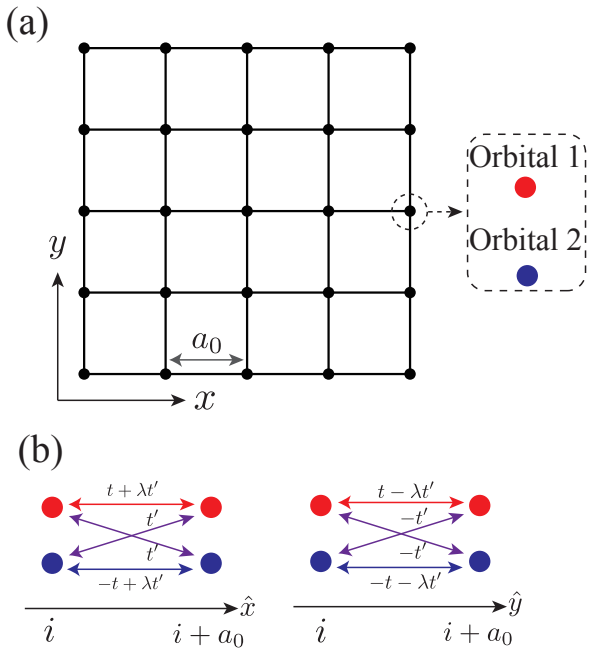

FIG. 1. Schematic figure of the tight-binding model of Eq. (3). (a) The lattice structures and (b) the hopping processes in x and y directions. The red and blue dots denote the orbital 1 and 2, respectively.

[*] mizoguchi@rhodia.ph.tsukuba.ac.jp

transport coefficients of all the three types in an equal-footing manner within the continuum model, which motivates us to study a lattice model.

In this paper, we study longitudinal transport coefficients of a simple lattice model with Dirac cones in two dimensions. The model is a generalization of the model proposed by one of the authors [48], where the type-III Dirac cone is realized. The slight modulation of the Hamiltonian enables us to control the type of Dirac cones by a single parameter, as we will show later. Therefore, the model serves as a minimal model of tilted Dirac cones in two dimensions.

For this model, we calculate the electric and thermoelectric transport coefficients on the basis of the Kubo formula [49, 50]. We consider the effects of nonmagnetic impurities by using the relaxation time approximation. Our result indicates that the largest thermoelectric response is obtained not for the type-III case but for the optimally tilted type-I case. This indicates that the thermoelectric transport coefficients of type-III Dirac fermions can not be regarded as a limiting case of either the type-I or the type-II. To be more specific, the transport coefficients of the type-III Dirac fermions are qualitatively similar to those of the type-I, in that the spectral conductivity shows a dip rather than a peak at the Dirac point for the type-I and the type-III cases, and that the sign of the Seebeck coefficient for the type-III case is the same as that for type-I case. However, the transport coefficients do not behave monotonically upon increasing the tilting. Quantitatively, for the optimal case, the sizable transport coefficients are obtained, e.g., the dimensionless figure of merit being 0.18 for the temperature of the order of 100 K under a trial setting of parameters.

The rest of this paper is structured as follows. In Sec. II, we introduce a model considered in this paper, namely, a square-lattice model with two internal degrees of freedom. The main results of this paper are presented in Sec. III. We first show the chemical potential dependence of the electric conductivity at zero temperature. Then we argue the temperature dependence of the Seebeck coefficient, and the power factor, and the dimensionless figure of merit. Finally, we present the results in the low temperature region based on the Mott formula, which are helpful for obtaining a deeper understanding about the comparison among the three types of Dirac cones. The summary of this paper is presented in Sec. IV.

We remark that, throughout this paper, $\hbar$ represents the reduced Planck constant and k_{B} represents the Boltzmann constant.

II. MODEL: TWO-ORBITAL SQUARE-LATTICE MODEL

To comprehensively study transport coefficients of Dirac fermions of all the three types on a lattice model, we introduce a simple tight-binding model defined on a square lattice. The model is an extension of one introduced in Ref. 48, where the type-III Dirac cones are selectively tailored. The model considered here is a spinless-fermion model. If we incorporate the spin degrees of freedom, the spectral conductivity of Eq. (8) is to be multiplied by two, thus the results of Sec. III are to be modified accordingly. The spinless fermions have two internal degrees of freedom, labeled by 1 and 2, which we will call the "orbital" henceforth [Fig. 1(a)].

Our tight-binding Hamiltonian is given as

$$H = \sum_{\langle i,j\rangle} \sum_{\eta_1,\eta_2=1,2} t_{i,j}^{\eta_1,\eta_2} c_{i,\eta_1}^{\dagger} c_{j,\eta_2} + (\mathrm{H.c.}), \tag{1}$$

where i and j denote the sites and $\langle\cdot,\cdot\rangle$ denotes the nearest-neighbor pair of sites. The hopping integrals $t_{i,j}^{\eta_1,\eta_2}$ are depicted in Fig. 1(b). We note that the hopping integrals in x direction are different from those in y direction. The momentum space representation is given as

$$H = \sum_{\boldsymbol{k}} \boldsymbol{\psi}_{\boldsymbol{k}}^{\dagger} \mathcal{H}(\boldsymbol{k}) \boldsymbol{\psi}_{\boldsymbol{k}}, \tag{2}$$

where $\boldsymbol{\psi}_{\boldsymbol{k}} = (c_{\boldsymbol{k},1}, c_{\boldsymbol{k},2})^{\mathrm{T}}$ denotes the annihilation operators of fermions with the crystal momentum $\boldsymbol{k}$ and

$$\mathcal{H}(\boldsymbol{k}) = \begin{pmatrix} \lambda a_{\boldsymbol{k}} + d_{\boldsymbol{k}} & a_{\boldsymbol{k}} \\ a_{\boldsymbol{k}} & \lambda a_{\boldsymbol{k}} - d_{\boldsymbol{k}} \end{pmatrix}. \tag{3}$$

Here we have introduced $a_{\boldsymbol{k}} := 2t' (\cos k_x a_0 - \cos k_y a_0)$ and $d_{\boldsymbol{k}} := 2t (\cos k_x a_0 + \cos k_y a_0)$, with a_0 being the lattice constant. The dimensionless parameter λ is real and nonnegative; the modification from $a_{\boldsymbol{k}}$ to $\lambda a_{\boldsymbol{k}}$ in the diagonal matrix elements is an extension compared with the previous work [48]. The schematic figure in the real space is depicted in Fig. 1.

For this model, the dispersion relations of two bands, $\varepsilon_{\boldsymbol{k},\pm}$, become

$$\varepsilon_{\boldsymbol{k},\pm} = \lambda a_{\boldsymbol{k}} \pm \sqrt{a_{\boldsymbol{k}}^2 + d_{\boldsymbol{k}}^2}. \tag{4}$$

In Figs. 2(b)-(d), we plot the dispersion relation of Eq. (4). Although the model is a toy model and thus the results will not apply to specific materials directly, it will be useful to set actual values of parameters so that we can roughly estimate the electric and thermoelectric coefficients. Therefore, in the rest of this paper, we set $t = -1$ eV and $t' = -0.3$ eV. We note that, if the hopping amplitude changes, then the other parameters μ, Γ, and T are to be scaled accordingly.

We find from Eq. (4) that, for any λ, the Dirac cones appear at the momenta where $a_{\boldsymbol{k}} = 0$ and $d_{\boldsymbol{k}} = 0$ are simultaneously satisfied, that are, $\boldsymbol{k} = \left(\pm\frac{\pi}{2a_0}, \pm\frac{\pi}{2a_0}\right)$ and $\boldsymbol{k} = \left(\pm\frac{\pi}{2a_0}, \mp\frac{\pi}{2a_0}\right)$. Importantly, the type of the Dirac cone can be tuned by a single parameter λ, as shown in Fig. 2. Clearly, we have the type-I (type-II) Dirac cones for $\lambda < 1$ ($\lambda > 1$); $\lambda = 1$ is the critical case, i.e., the type-III Dirac cones, as pointed out in Ref. 48. This enables us to study the transport coefficients of three types of Dirac cones comprehensively on this lattice model.

To further clarify the difference among thee types, we depict the shape of Fermi surface for $\mu = 0$ eV in Figs. 2(e)-(g). For $\lambda = 0.5$, i.e., for the tilted type-I Dirac cone, the Fermi surface corresponds to the Dirac points. For $\lambda = 1.5$, i.e., for the type-II Dirac cone, the Fermi surface has a finite area in the Brillouin zone, [Fig. 2(g)] and it consists of two species

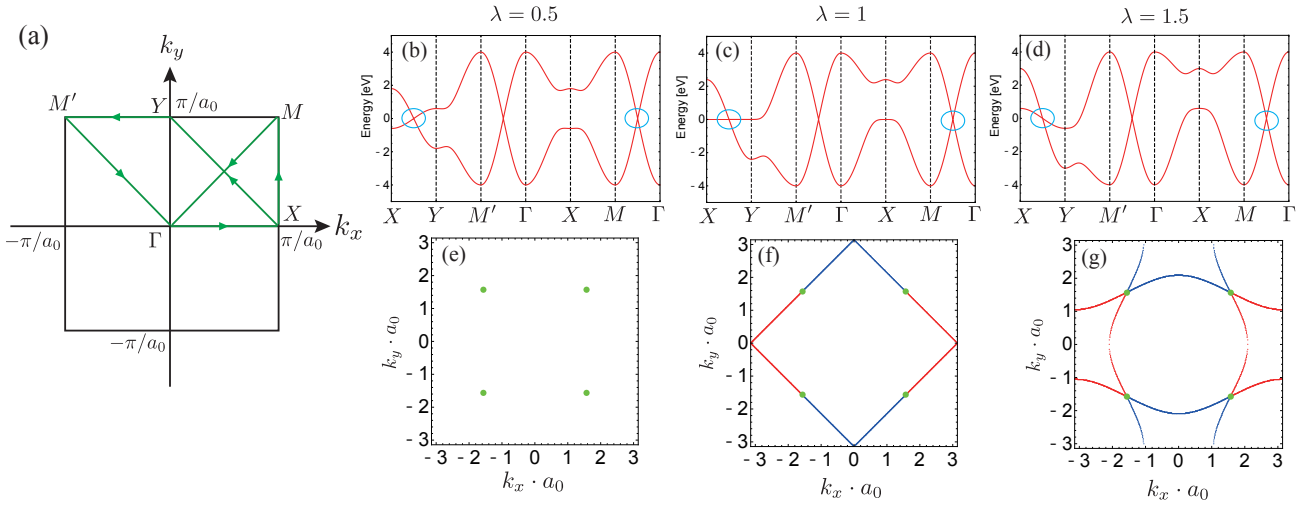

FIG. 2. (a) The first Brillouin zone. The green lines correspond to the high-symmetry lines on which we plot the band structure in (b)-(d). Band structures for the Hamiltonian of Eq. (3) with $t = -1$ eV, $t' = -0.3$ eV and (b) $\lambda = 0.5$, (c) $\lambda = 1$, and (d) $\lambda = 1.5$. The horizontal axis denotes $\boldsymbol{k}$. The Dirac cone at $\boldsymbol{k} = \left(\frac{\pi}{2a_0}, \frac{\pi}{2a_0}\right)$ are encircled by cyan circles. The Fermi surface at $\mu = 0$ eV for (e) $\lambda = 0.5$, (f) $\lambda = 1$, and (g) $\lambda = 1.5$. The green dots represent the Dirac points. Red and blue dots are the electron-type surface (i.e., $\varepsilon_{\boldsymbol{k},+} = \mu$) and the hole-type surface (i.e., $\varepsilon_{\boldsymbol{k},-} = \mu$), respectively.

of surfaces, namely, the electron-type surface and hole-type surface, which meet each other at the Dirac points. For $\lambda = 1$ i.e., for the type-III Dirac cone [Fig. 2(f)], the Fermi surface shrinks compared with that in Fig. 2(g) and forms the straight lines ($k_x \pm k_y = \pi/a_0, -\pi/a_0$).

In Fig. 3, we plot the DOS defined as

$$\rho(\epsilon) = -\frac{1}{\pi}\sum_{\boldsymbol{k}} \mathrm{Im}\left[\frac{1}{\epsilon + i\eta - \varepsilon_{\boldsymbol{k},+}} + \frac{1}{\epsilon + i\eta - \varepsilon_{\boldsymbol{k},-}}\right], \quad (5)$$

where η is a small parameter, being set to $0.01|t|$. For $\lambda = 0.5$, i.e., for the tilted type-I Dirac cone, DOS drops at $\epsilon = 0$, reflecting the fact that the Fermi surface consists of the Dirac points. For $\lambda = 1.5$, i.e., for the type-II Dirac cone, DOS becomes finite at $\epsilon = 0$, since the Fermi surface is no longer the points. For $\lambda = 1$ i.e., for the type-III Dirac cone, a sharp peak of DOS at $\epsilon = 0$ appears, due to a directionally-flat dispersion at zero energy. Away from $\epsilon \sim 0$, we see several peaks for all cases, e.g., $\epsilon = 0.5$ eV and 2 eV for $\lambda = 0.5$. They originate from the quasi-flat dispersion near X and Y points, as shown in Fig. 2(b).

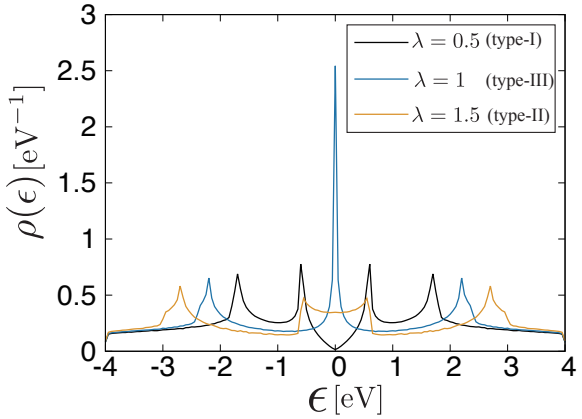

FIG. 3. Density of states for the model of Eq. (3).

III. RESULTS

A. Longitudinal electric conductivity

We first calculate the electric longitudinal conductivity. The conductivity tensor $\overleftrightarrow{\sigma}$ is defined as

$$\boldsymbol{j} = \overleftrightarrow{\sigma}\boldsymbol{E}, \quad (6)$$

where $\boldsymbol{j}$ is the current density and $\boldsymbol{E}$ is the electric field. The longitudinal conductivity corresponds to the diagonal element of the conductivity tensor, which we write σ_{ii} ($i = x, y$). We have confirmed that relation $\sigma_{xx} = \sigma_{yy}$ holds (see Appendix A for the proof), so we focus on σ_{xx} henceforth. Note that the above relation implies that the anisotropy of the conductivity is not observed in this model, unlike the case of the continuum model with a single tilted Dirac cone [28–30, 41]. This might originate from the fact that there are two pairs of Dirac cones, namely, $\boldsymbol{k} = \left(\pm\frac{\pi}{2a_0}, \pm\frac{\pi}{2a_0}\right)$ and $\boldsymbol{k} = \left(\pm\frac{\pi}{2a_0}, \mp\frac{\pi}{2a_0}\right)$, whose tilting direction is perpendicular to each other.

The longitudinal conductivity can be calculated by using the Kubo formula:

$$\sigma_{xx} = -\int_{-\infty}^{\infty} d\epsilon\, f'(\epsilon - \mu)\alpha_{xx}(\epsilon), \quad (7)$$

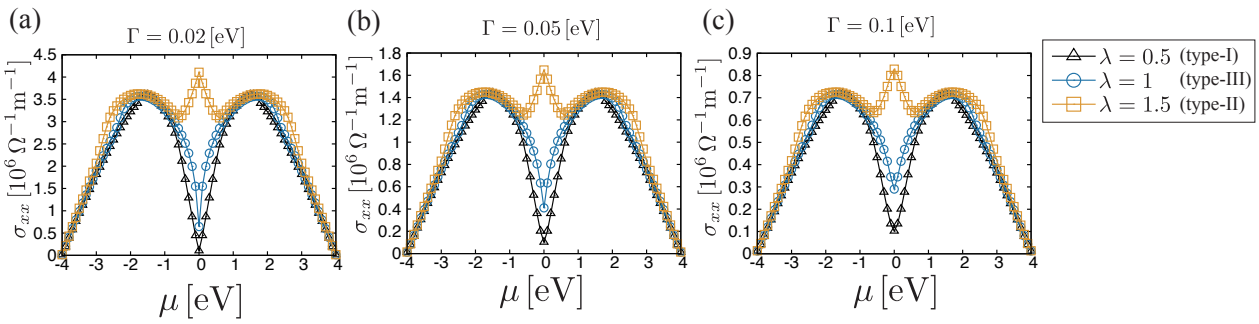

FIG. 4. Longitudinal conductivity for (a) $\Gamma = 0.02$ eV, (b) $\Gamma = 0.05$ eV, and (c) $\Gamma = 0.1$ eV.

where μ is the chemical potential and $\alpha_{xx}(\epsilon)$ is referred to as the spectral conductivity:

$$\alpha_{xx}(\epsilon) = \frac{\hbar e^2}{2\pi A d_0} \sum_{\boldsymbol{k}} \mathrm{Tr}\{G^{(R)}(\boldsymbol{k},\epsilon)v_x(\boldsymbol{k})G^{(A)}(\boldsymbol{k},\epsilon)v_x(\boldsymbol{k}) - \mathrm{Re}\left[G^{(R)}(\boldsymbol{k},\epsilon)v_x(\boldsymbol{k})G^{(R)}(\boldsymbol{k},\epsilon)v_x(\boldsymbol{k})\right]\}. \quad (8)$$

Here, $-e$ is the charge of an electron, A is the area of the two-dimensional layer, $f(\epsilon) = 1/(e^{\beta\epsilon}+1)$ is the Fermi-Dirac distribution function ($\beta = 1/k_{\mathrm{B}}T$), and $f'(\epsilon)$ is its derivative. In Eq. (8), we have included an interlayer distance d_0 to make $\alpha_{xx}(\epsilon)$ to have the unit for the three-dimensional (bulk) conductivity. This means that, although the tight-binding model of Eq. (2) is two-dimensional, we consider the quasi-two-dimensional (q-2D) system where the independent two-dimensional layers are stacked with the interlayer distance d_0. Such a q-2D nature applies to q-2D organic materials in which the tilted Dirac electrons are realized and the electric and thermoelectric transport coefficients are measured for bulk (3D) samples. Hereafter, we set $d_0 = 10\mathring{A}$ as a typical value of the q-2D materials. Note that we have neglected the interlayer coupling. In general, depending on the symmetries, the Dirac cones can acquire a mass gap due to the interlayer coupling. Nevertheless, regardless of the existence of such a mass gap, a small interlayer coupling does not change the following results qualitatively for temperatures being greater than the interlayer coupling.

As for the retarded and advanced Green's functions, $G^{(R)}(\boldsymbol{k},\epsilon)$ and $G^{(A)}(\boldsymbol{k},\epsilon)$, respectively, we employ the relaxation time approximation:

$$G^{(R)}(\boldsymbol{k},\epsilon) = [\epsilon + i\Gamma - \mathcal{H}(\boldsymbol{k})]^{-1}, \quad (9)$$

and

$$G^{(A)}(\boldsymbol{k},\epsilon) = [\epsilon - i\Gamma - \mathcal{H}(\boldsymbol{k})]^{-1}, \quad (10)$$

with Γ being the damping rate caused by the impurity scattering; we do not consider the screening effect of the impurity potential that causes the momentum and frequency dependence of Γ [51, 52]. We consider three cases, namely, $\Gamma = 0.02$ eV, 0.05 eV, and 0.1 eV. The velocity $v_x(\boldsymbol{k})$ is given as

$$v_x(\boldsymbol{k}) = \frac{1}{\hbar}\frac{\partial \mathcal{H}(\boldsymbol{k})}{\partial k_x}. \quad (11)$$

For the numerical calculations, we set $T = 0$, where $f'(\epsilon) = -\delta(\epsilon)$ thus $\sigma_{xx} = \alpha(\mu)$. Then we numerically take the summation over $\boldsymbol{k}$ with 800×800 meshes for $\Gamma = 0.02$ eV, 400×400 meshes for $\Gamma = 0.05$ eV, and 200×200 meshes for $\Gamma = 0.1$ eV.

In Fig. 4(a)-(c), we show the μ dependence of σ_{xx}. Three panels are for different values of Γ. Although Γ affects σ_{xx} quantitatively, the overall features of μ-dependence do not change. We see that the conductivity sharply drops for $\mu \to 0$ eV for $\lambda = 0.5$ (the type-I case) and $\lambda = 1$ (the type-III case), while it has a peak at $\mu = 0$ eV for $\lambda = 1.5$ (the type-II case). In this sense, the conductivity for the type-III case is similar to the type-I, rather than the type-II.

To account for this result, we compare the μ dependence of σ_{xx} with the DOS profile of Fig. 3. In general, the finite DOS is essential to obtain the sizable conductivity. In this respect, the results for the types-I and II coincide with the DOS profile, namely, the DOS approaches to zero (finite) at $\mu = 0$ eV for the type-I (II), which is reflected in the μ dependence of σ_{xx}. In contrast, for the type-III case, the conductivity shows a dip at $\mu = 0$ eV despite the peak of the DOS. This means that the directionally flat dispersion of the type-III Dirac cone, which leads to the peak of the DOS, does not contribute the conductivity probably because of the momentum dependence of the velocity operator that is another key factor for determination of the conductivity. Such a subtle interplay between the DOS profile and the momentum dependence of the velocity operator may also lead to the peak at $\mu = 0$ eV for the type-II Dirac cone.

B. Thermoelectric transport coefficients

Next, we calculate the Seebeck coefficient, [50, 53–55] the power factor, and the dimensionless figure of merit. The definitions of these quantities are as follows. We focus on the electric and thermal currents as well as the electric field and the temperature gradient are all in x direction. The electric current in the presence of the electric field and the temperature gradient is given as

$$j_x = L_{11}E_x + L_{12}\left(-\frac{\partial_x T}{T}\right), \quad (12)$$

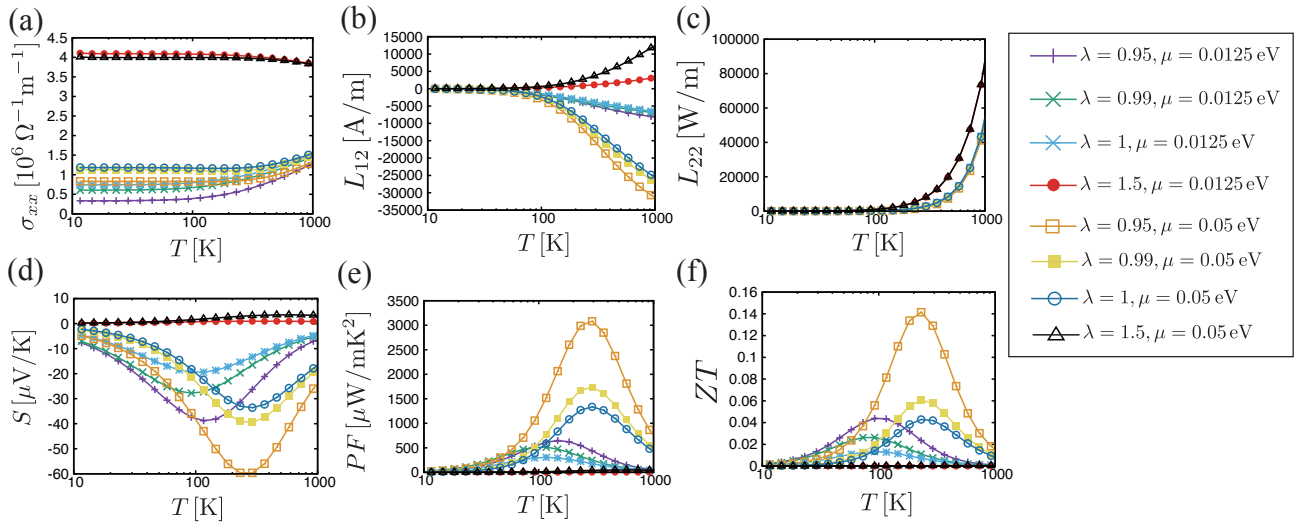

FIG. 5. Temperature dependence of (a) the conductivity, (b) L_{12}, (c) L_{22}, (d) the Seebeck coefficient, (e) the power factor, and (f) the dimensionless figure of merit. We set $\Gamma = 0.02$ eV.

and the thermal current is given as

$$j_Q^x = L_{21}E_x + L_{22}\left(-\frac{\partial_x T}{T}\right), \tag{13}$$

with $\partial_x T$ being the temperature gradient in x direction. Note that $L_{11} = \sigma_{xx}$, and $L_{12} = L_{21}$ due to the Onsager's relation. The Seebeck coefficient (S) is expressed by using L_{ij} $(i, j = 1, 2)$ as

$$S = \frac{1}{T}\frac{L_{12}}{L_{11}}. \tag{14}$$

The power factor (PF) and the dimensionless figure of merit (ZT) are defined as

$$PF = \frac{1}{T^2}\frac{L_{12}^2}{L_{11}}, \tag{15}$$

and

$$ZT = \frac{S^2\sigma}{\kappa}T, \tag{16}$$

respectively, where κ is the thermal conductivity. Generally, κ is given by $\kappa = \kappa_e + \kappa_{\mathrm{ph}}$, and κ_e (κ_{ph}) is the electronic (phonon) contribution to thermal conductivity. In this paper, we ignore κ_{ph} and calculate ZT using κ_e given by

$$\kappa_e = \frac{L_{22} - (L_{12}L_{21})/L_{11}}{T}. \tag{17}$$

Thus, the obtained results for ZT is maximum of the possible ZT. Note that the validity of neglecting the phonon contribution depends on the actual materials. For instance, in graphene, the phonon contribution is dominant [56].

In the present model, there are only the impurity scattering potentials that cause the damping rate, Γ. Therefore L_{12} is given by [55, 57, 58]

$$L_{12} = \frac{1}{e}\int_{-\infty}^{\infty} d\epsilon\,(\epsilon - \mu)f'(\epsilon - \mu)\alpha_{xx}(\epsilon), \tag{18}$$

with $\alpha_{xx}(\epsilon)$ being defined as in Eq. (8). This relation between L_{11} and L_{12} is called the Sommerfeld-Bethe relation [59]. It is to be noted that we consider only the electric contribution to Seebeck coefficient and neglect the other contributions such as the phonon drag deriving from the electron-phonon interaction [55, 60]. Similarly, L_{22} is calculated as

$$L_{22} = -\frac{1}{e^2}\int_{-\infty}^{\infty} d\epsilon\,(\epsilon - \mu)^2 f'(\epsilon - \mu)\alpha_{xx}(\epsilon). \tag{19}$$

We perform ϵ integration in Eqs. (7), (18), and (19) numerically, and calculate S, PF and ZT by using L_{11}, L_{12}, and L_{22} thus obtained. In the actual numerical calculation, we limit the interval of the integration to $\epsilon \in [-1, 1]$ (eV) in Eqs. (7), (18), and (19), and perform the integration numerically with the number of meshes of ϵ being 960. In this subsection, the damping rate Γ is set to be 0.02 eV.

The results are shown in Fig. 5(a)-(f). Eight lines are for the different combinations of λ and μ. Note that we do not consider the temperature dependence of μ but we set it as a parameter. We see that for $\lambda \sim 1$, all of three quantities have peaks at temperatures in the order of 100 K. In fact, for $\lambda \leq 1$, S, PF, and ZT have a maximum at $T \sim \mu/2k_{\mathrm{B}}$. For S and ZT, this fact can be accounted for by the linear dependence of $\alpha_{xx}(\epsilon)$ as a function of ϵ; see Appendix B for details.

Among the combinations of λ and μ shown in Fig. 5(d)-(f), the case of $\lambda = 0.95$ and $\mu = 0.05$ eV exhibits the largest response. The results indicate that there exists an optimal degree of tilting and carrier density to obtain the large thermoelectric responses. We also see that, in deep inside the type-II case ($\lambda = 1.5$), the thermoelectric response functions are small compared with those for $\lambda \sim 1$. Note that, for the type-II case, a dominant contribution to the Seebeck coefficient comes from the region near the Dirac points; see Appendix C for further details.

To further study the optimal tilting for the large thermoelectric response, we investigate the λ dependence of S, PF,

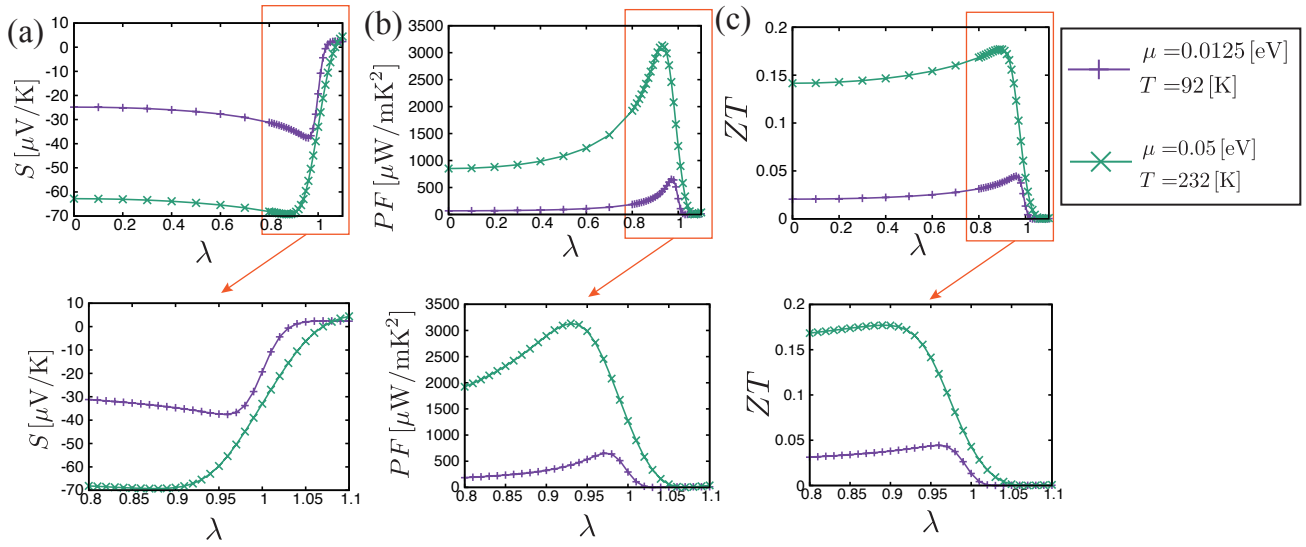

FIG. 6. λ dependence of (a) the Seebeck coefficient, (b) the power factor, and (c) the dimensionless figure of merit. We set $\Gamma = 0.02$ eV.

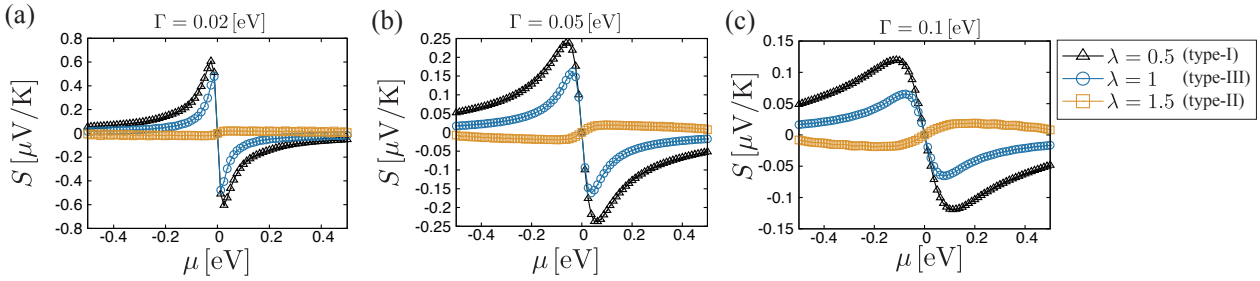

FIG. 7. Seebeck coefficient at $T = 1.16$K for (a) $\Gamma = 0.02$ eV, (b) $\Gamma = 0.05$ eV, and (c) $\Gamma = 0.1$ eV.

and ZT. The results are shown in Fig. 6(a)-(c). The temperatures are set to be $T = 92$ K and 232 K for $\mu = 0.0125$ eV and 0.05 eV, respectively, where the peaks are realized in Fig. 5(d)-(f). We see that the optimal tilting parameter λ indeed exists, which is slightly smaller than $\lambda = 1$. We also see that, for all of the three quantities, their absolute values for $\mu = 0.05$ eV are larger than those for $\mu = 0.0125$ eV. However, as we will argue in the next subsection, they do not increase monotonically as a function of μ. Rather, there also exists an optimal value of μ, as we will explain in the next subsection. Therefore, for the large thermoelectric response, the suitable electronic structure is the type-I Dirac cone which is very vicinity of the type-III Dirac cone. The carrier density (or the chemical potential) is also to be tuned at the optimal value. At the maximum within the present results ($\mu = 0.05$ eV and $\lambda = 0.89$), we obtain $S \sim -70\,\mu\mathrm{V/K}$, $PF \sim 3000\,\mu\mathrm{W/mK^2}$, and $ZT \sim 0.18$, which are sizable values.

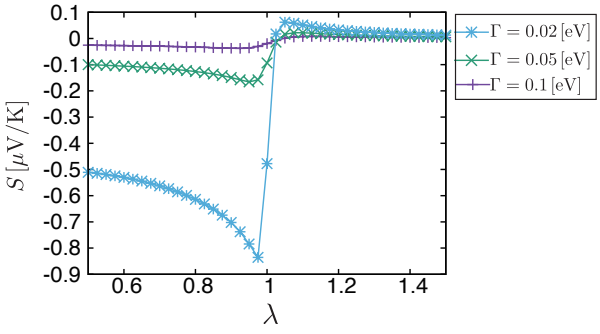

FIG. 8. λ dependence of the Seebeck coefficient at $T = 1.16$K and $\mu = 0.0125$ eV.

C. Low temperatures

To understand the physical origin of large Seebeck coefficient and large ZT, it is useful to study their low-temperature behaviors. To this end, for L_{12}, we apply the Sommerfeld expansion to Eq. (18). Then, we find that, for low temperatures, S is given by the Mott formula [61],

$$S = -\frac{\pi^2}{3}\frac{k_{\mathrm{B}}^2 T}{e}\left(\frac{d\ln\alpha_{xx}(\epsilon)}{d\epsilon}\right)_{\epsilon=\mu}. \tag{20}$$

In Fig. 7(a)-(c), we show the μ dependence of S obtained from the Mott formula for $\mu \in [-0.5, 0.5]$. We set the tem-

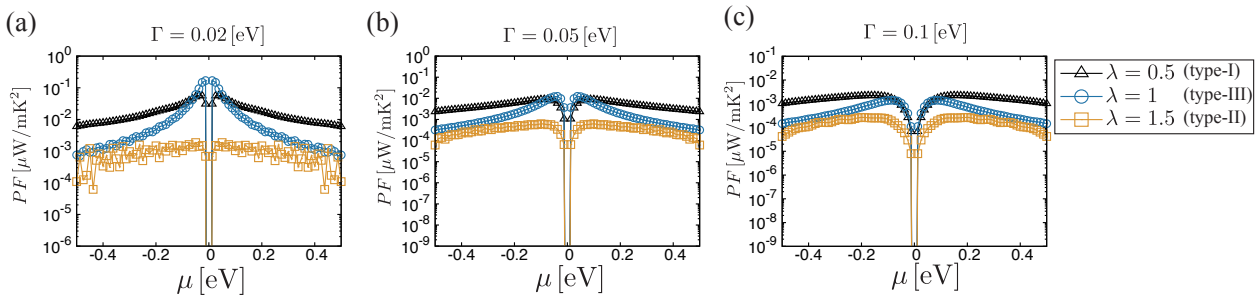

FIG. 9. μ dependence of the power factor at $T = 1.16$ K for (a) $\Gamma = 0.02$ eV, (b) $\Gamma = 0.05$ eV, and (c) $\Gamma = 0.1$ eV.

perature to be small but finite, as $T = 1.16$ K (i.e., $k_{\rm B}T = 10^{-4}|t|$). We see that S is vanishing when μ is right at the Dirac point for all the three types, as S is the odd function of μ. Comparing among three types, we find that the type-I and type-III cases have large S, while the type-II case has small S. This can be accounted for by the fact that the conductivity (or L_{11}) is large for the type-II case.

We also find that the sign of S in the type-I and type-III case is opposite to that for the type II. For instance, for positive μ, S is negative for $\lambda = 0.5$ and 1, while S is positive for $\lambda = 1.5$. To further clarify the nature of the sign change, we plot the λ dependence of S at $\mu = 0.0125$ eV in Fig. 8. As λ approaches to 1 from the type-I region, S is negative and $|S|$ becomes larger. At $\lambda = 1$, i.e., the type-III case, S is still negative but $|S|$ decreases. This indicates the non-monotonic behavior of S upon increasing the tilting of the Dirac cones from the type-I side. Then, the sign change of S occurs for $\lambda = \lambda_{\rm c}$ with $\lambda_{\rm c} > 1$. Note that this behavior is also seen in the finite temperatures, as shown in Fig. 6(a). The result can be understood as follows. From Eqs. (7) and (20), one finds that S is proportional to the μ-derivative of σ at $T = 0$. Then, the sign of S, which is equal to that of L_{12}, is dictated by whether σ at $\mu = 0$ is a dip or a peak. Clearly, the types-I and III show a dip while the type-II show a peak, which coincides with the resulting sign of S.

Next, we present the results of the power factor. To estimate the low-temperature behavior, we again employ the Sommerfeld expansion to L_{12}. In Fig. 9(a)-(c), we show the μ dependence of PF. As clearly seen, the large power factor is obtained in the types I and III for small but finite μ. In particular, the power factor for the type-III Dirac system is the largest among three types for $\Gamma = 0.02, 0.05$ eV with $|\mu| \lesssim 0.05$ eV, due to the subtle competition between L_{12} and L_{11}.

IV. SUMMARY

In this paper, we have investigated the electric and thermoelectric transport coefficients of a two-orbital square-lattice model of Eq. (3). In this model, the type of Dirac cones can be tuned by a single parameter, λ, and thus the model serves as a minimal model for studying transport phenomena.

We have computed the electric conductivity, the Seebeck coefficient, the power factor, and the dimensionless figure of merit, on the basis of the Kubo formula and the relaxation time approximation. We have found that the transport coefficients of the type-III case can not be regarded as a simple limit of the type-I nor type-II. Actually, there exists an optimal degree of tilting and chemical potential to obtain the largest thermoelectric responses within the type-I regime; the type-III Dirac cone is not the optimal case. Furthermore, the chemical potential should not be right at the Dirac point. The best chemical potential for the large Seebeck coefficient will be near $\mu \sim 0.05$eV. As for the temperature dependence, the peaks appear at $T \sim \mu/2k_{\rm B}$. For the optimal case within our results, sizable transport coefficients are obtained, e.g., the dimensionless figure of merit being 0.18.

To understand the physical origin of the above behaviors, we also study the low-temperature behaviors by using the Mott formula. We have found that the sign of the Seebeck coefficient for the type-III case is the same as that for type-I case. This originates from the fact that the spectral conductivity shows a dip rather than a peak at $\epsilon = 0$.

Finally, we address the possible implications to the real materials. The type-I Dirac cones with large tilting in quasi-two dimensions are realized in organic conductors such as α-(BEDT-TTF)$_2$I$_3$ [5, 7–10] and α-(BEST)$_2$I$_3$ [62–64]. For α-(BEDT-TTF)$_2$I$_3$, the measurements of the Seebeck coefficients were indeed reported [65, 66]. Further interestingly, the degree of titling can be tuned by applying the pressure [5, 67, 68]. Therefore, these materials will be candidates for testing the tilting dependence of the thermoelectric transport coefficients.

ACKNOWLEDGMENTS

We thank I. Tateishi and S. Ozaki for fruitful discussions and comments. T. M. thanks Y. Hatsugai for the collaboration in the prior work (Ref. [48]). This work is supported by JSPS KAKENHI, Grants No. JP18H01162, No. JP18K03482, No. JP19K03720, and No. JP20K03802, and by JST-Mirai Program, Grant No. JPMJMI19A1. T. M. is supported by JSPS KAKENHI, Grant No. JP20K14371.

Appendix A: Proof for $\sigma_{xx} = \sigma_{yy}$

In this appendix, we show a proof of the relation $\sigma_{xx} = \sigma_{yy}$ in the present model. Note that C_4 symmetry is broken in this model, thus the above relation is not obtained straightforwardly.

Let $\alpha_{yy}(\epsilon)$ be the spectral conductivity for y direction, i.e., $\alpha_{yy}(\epsilon)$ is obtained by replacing $v_x(\boldsymbol{k})$ with $v_y(\boldsymbol{k})$ in Eq. (8), as

$$\alpha_{yy}(\epsilon) = \frac{\hbar e^2}{2\pi A d_0}\sum_{\boldsymbol{k}} \mathrm{Tr}\{G^{(R)}(\boldsymbol{k},\epsilon)v_y(\boldsymbol{k})G^{(A)}(\boldsymbol{k},\epsilon)v_y(\boldsymbol{k}) - \mathrm{Re}\left[G^{(R)}(\boldsymbol{k},\epsilon)v_y(\boldsymbol{k})G^{(R)}(\boldsymbol{k},\epsilon)v_y(\boldsymbol{k})\right]\}. \tag{A1}$$

In the following, we show that $\alpha_{xx}(\epsilon) = \alpha_{yy}(\epsilon)$ holds. For simplicity of writing, we set $a_0 = 1$ in this appendix.

To begin with, show that the spectral conductivity is an even function of ϵ, i.e., $\alpha_{xx}(\epsilon) = \alpha_{xx}(-\epsilon)$ holds. To this aim, we first point out that $\mathcal{H}(k_x, k_y)$ satisfies

$$\mathcal{H}(k_x+\pi, k_y+\pi) = -\mathcal{H}(k_x, k_y). \tag{A2}$$

Therefore, we have

$$v_x(k_x+\pi, k_y+\pi) = -v_x(k_x, k_y), \tag{A3}$$

and

$$\begin{aligned} G^{(R)}(k_x+\pi, k_y+\pi, \epsilon) &= [(\epsilon+i\Gamma) - \mathcal{H}(k_x+\pi, k_y+\pi)]^{-1} \\ &= -[(-\epsilon - i\Gamma) - \mathcal{H}(k_x, k_y)]^{-1} \\ &= -G^{(A)}(k_x, k_y, -\epsilon). \end{aligned} \tag{A4}$$

Substituting Eqs. (A3) and (A4) into Eq. (8) and changing the variable as $k_x \to k_x - \pi$ and $k_y \to k_y - \pi$, we have

$$\begin{aligned} \alpha_{xx}(\epsilon) &= \sum_{k_x,k_y} \frac{\hbar e^2}{2\pi A d_0}\mathrm{Tr}\{G^{(R)}(k_x,k_y,\epsilon)v_x(k_x,k_y)G^{(A)}(k_x,k_y,\epsilon)v_x(k_x,k_y) \\ &- \mathrm{Re}\left[G^{(R)}(k_x,k_y,\epsilon)v_x(k_x,k_y)G^{(R)}(k_x,k_y,\epsilon)v_x(k_x,k_y)\right]\} \\ &= \sum_{k_x,k_y} \frac{\hbar e^2}{2\pi A d_0}\mathrm{Tr}\{G^{(R)}(k_x+\pi,k_y+\pi,\epsilon)v_x(k_x+\pi,k_y+\pi)G^{(A)}(k_x+\pi,k_y+\pi,\epsilon)v_x(k_x+\pi,k_y+\pi) \\ &- \mathrm{Re}\left[G^{(R)}(k_x+\pi,k_y+\pi,\epsilon)v_x(k_x+\pi,k_y+\pi)G^{(R)}(k_x+\pi,k_y+\pi,\epsilon)v_x(k_x+\pi,k_y+\pi)\right]\} \\ &= \sum_{k_x,k_y} \frac{\hbar e^2}{2\pi A d_0}\mathrm{Tr}\{G^{(A)}(k_x,k_y,-\epsilon)v_x(k_x,k_y)G^{(R)}(k_x,k_y,-\epsilon)v_x(k_x,k_y) \\ &- \mathrm{Re}\left[G^{(A)}(k_x,k_y,-\epsilon)v_x(k_x,k_y)G^{(A)}(k_x,k_y,-\epsilon)v_x(k_x,k_y)\right]\} \\ &= \alpha_{xx}(-\epsilon). \end{aligned} \tag{A5}$$

Note that we have used $G^{(A)}(k_x,k_y,\epsilon) = [G^{(R)}(k_x,k_y,\epsilon)]^*$ and $v_x^*(k_x,k_y) = v_x(k_x,k_y)$, which lead to $\mathrm{Re}\left[G^{(A)}(k_x,k_y,\epsilon)v_x(k_x,k_y)G^{(A)}(k_x,k_y,\epsilon)v_x(k_x,k_y)\right] = \mathrm{Re}\left[G^{(R)}(k_x,k_y,\epsilon)v_x(k_x,k_y)G^{(R)}(k_x,k_y,\epsilon)v_x(k_x,k_y)\right]$.

Next, we show that $\alpha_{yy}(\epsilon) = \alpha_{xx}(-\epsilon)$. To show this, we point out that $\mathcal{H}(k_x, k_y)$ satisfies

$$\mathcal{H}(k_x, k_y) = -\tau_x \mathcal{H}(k_y, k_x)\tau_x, \tag{A6}$$

where τ_x is the x component of the Pauli matrix. Then, we have

$$\begin{aligned} v_y(k_x,k_y) &= \frac{1}{\hbar}\frac{\partial \mathcal{H}(k_x,k_y)}{\partial k_y} = -\frac{1}{\hbar}\tau_x\frac{\partial \mathcal{H}(k_y,k_x)}{\partial k_y}\tau_x \\ &= -\tau_x v_x(k_y,k_x)\tau_x, \end{aligned} \tag{A7}$$

and

$$\begin{aligned} G^{(R)}(k_x,k_y,\epsilon) &= [(\epsilon+i\Gamma) - \mathcal{H}(k_x,k_y)]^{-1} \\ &= -\{\tau_x[(-\epsilon - i\Gamma) - \mathcal{H}(k_y,k_x)]\tau_x\}^{-1} \\ &= -\tau_x G^{(A)}(k_y,k_x,-\epsilon)\tau_x. \end{aligned} \tag{A8}$$

Substitute Eqs. (A7) and (A8) into Eq. (A1) and changing the variable as $k_x \to k_y$ and $k_y \to k_x$, we have

$$\begin{aligned}\alpha_{yy}(\epsilon) &= \sum_{k_x,k_y} \frac{\hbar e^2}{2\pi A d_0} \mathrm{Tr}\{G^{(R)}(k_x,k_y,\epsilon)v_y(k_x,k_y)G^{(A)}(k_x,k_y,\epsilon)v_y(k_x,k_y) \\ &- \mathrm{Re}\left[G^{(R)}(k_x,k_y,\epsilon)v_y(k_x,k_y)G^{(R)}(k_x,k_y,\epsilon)v_y(k_x,k_y)\right]\} \\ &= \sum_{k_x,k_y} \frac{\hbar e^2}{2\pi A d_0} \mathrm{Tr}\{\tau_x G^{(A)}(k_y,k_x,-\epsilon)v_x(k_y,k_x)G^{(R)}(k_y,k_x,-\epsilon)v_x(k_y,k_x)\tau_x \\ &- \mathrm{Re}\left[\tau_x G^{(A)}(k_y,k_x,-\epsilon)v_x(k_y,k_x)G^{(A)}(k_y,k_x,-\epsilon)v_x(k_y,k_x)\tau_x\right]\} \\ &= \sum_{k_x,k_y} \frac{\hbar e^2}{2\pi A d_0} \mathrm{Tr}\{\tau_x G^{(A)}(k_x,k_y,-\epsilon)v_x(k_x,k_y)G^{(R)}(k_x,k_y,-\epsilon)v_x(k_x,k_y)\tau_x \\ &- \mathrm{Re}\left[\tau_x G^{(A)}(k_x,k_y,-\epsilon)v_x(k_x,k_y)G^{(A)}(k_x,k_y,-\epsilon)v_x(k_x,k_y)\tau_x\right]\} \\ &= \alpha_{xx}(-\epsilon). \end{aligned} \tag{A9}$$

To obtain the final line of Eq. (A9), we have used the fact that the trace is invariant under cyclic permutations.

Combining (A5) and (A9), we find $\alpha_{xx}(\epsilon) = \alpha_{yy}(\epsilon)$, which leads to $\sigma_{xx} = \sigma_{yy}$.

Appendix B: Peak temperature of the Seebeck coefficient and figure of merit for the types-I and III Dirac fermions

In this appendix, we elucidate the origin of the peak temperature of S, using the evaluation method proposed by Mahan and Sofo [69]. Note that the same argument was presented in Ref. 70 for the conventional Dirac fermion system. From Eqs. (7), (18) and (19), we find

$$L_{11} = \int_{-\infty}^{\infty} dw\, g_0(w)\alpha_{xx}(w/\beta+\mu), \tag{B1}$$

$$L_{12} = -\frac{1}{e\beta}\int_{-\infty}^{\infty} dw\, g_1(w)\alpha_{xx}(w/\beta+\mu), \tag{B2}$$

and

$$L_{22} = \frac{1}{e^2\beta^2}\int_{-\infty}^{\infty} dw\, g_2(w)\alpha_{xx}(w/\beta+\mu), \tag{B3}$$

where $w := \beta(\epsilon-\mu)$ and

$$g_n(w) = \frac{w^n e^w}{(e^w+1)^2}. \tag{B4}$$

Note that $g_n(w)$ is an odd (even) function of w if n is odd (even).

Hereafter, we assume that μ is positive for simplicity. For analytical estimation of L_{11}, L_{12} and L_{22}, we assume a simple analytic form of the spectral conductivity. Specifically, from the numerical results in Fig. 4, for the types-I and III Dirac systems, the spectral conductivity around $\epsilon = 0$ can be approximated as

$$\alpha_{xx}(\epsilon) \sim \alpha_0 + \alpha_1|\epsilon|, \tag{B5}$$

where α_0 and α_1 are coefficients. Substituting Eq. (B5) into Eqs. (B1) and (B3) and recalling the definition of S in Eq. (14), we find

$$S = -\frac{k_\mathrm{B}}{e}\cdot\frac{2\alpha_1\mu h_1(-w_0)+\alpha_1 k_\mathrm{B}T h_2(-w_0)}{\alpha_0+2\alpha_1 k_\mathrm{B}T h_1(-w_0)+\alpha_1\mu h_0(-w_0)}. \tag{B6}$$

Here, $w_0 := -\mu/(k_\mathrm{B}T)$ and the functions $h_n(w)$ ($n = 0,1,2$) are given as

$$h_0(w) = \int_{-w}^{w} dw'\, g_0(w') = \tanh\frac{w}{2}, \tag{B7a}$$

$$h_1(w) = \int_{w}^{\infty} dw'\, g_1(w') = \log(1+e^w) - \frac{we^w}{e^w+1}, \tag{B7b}$$

and

$$\begin{aligned} h_2(w) &= \int_{-w}^{w} dw'\, g_2(w') \\ &= \frac{2w^2e^w}{e^w+1} - 4w\log(1+e^w) - 4\mathrm{Li}_2(-e^w) - \frac{\pi^2}{3}. \end{aligned} \tag{B7c}$$

Note that the integration range of w in Eqs. (B1) and (B3) runs over $w \in [-\infty,\infty]$, where the approximation of (B5) breaks down. Nevertheless, using (B5) is valid as long as μ is close to 0, because $g_n(w)$ decays rapidly as $|w| \to \infty$.

Further, Fig. 4 indicates that, in the clean limit (i.e, when Γ is sufficiently small), α_0 in the spectral conductivity becomes less dominant. Hence, we set $\alpha_0 \to 0$ for simplicity. By doing so, we have

$$\begin{aligned} S &\sim \frac{k_\mathrm{B}}{e}\cdot X(w_0), \\ X(w_0) &= -\frac{h_2(-w_0)-2w_0h_1(-w_0)}{2h_1(-w_0)-w_0h_0(-w_0)}, \end{aligned} \tag{B8}$$

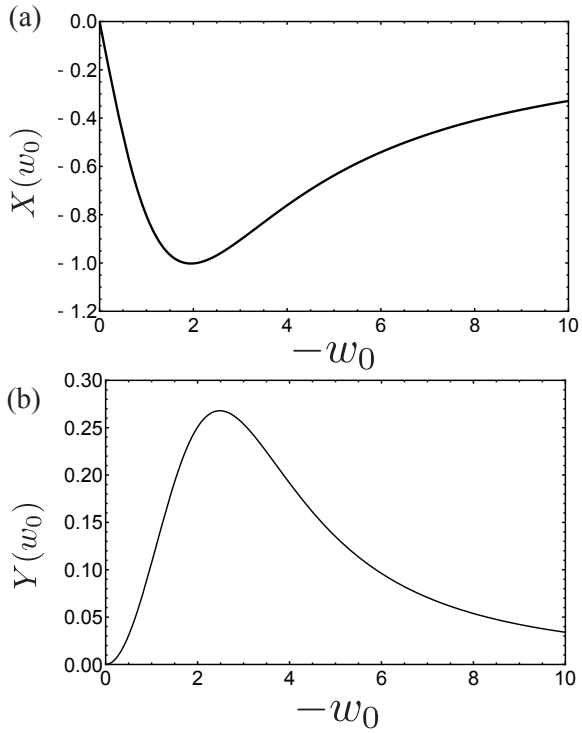

FIG. 10. (a) $X(w_0)$ of Eq. (B8) and (b) $Y(w_0)$ of Eq. (B9) as a function of $-w_0$. Note that w_0 is negative when μ is positive.

which does not depend on α_1. Equation (B8) indicates that the temperature and chemical potential dependence of S is determined by the single variable $w_0 = -\mu/(k_{\rm B}T)$.

Figure 10(a) shows the function $X(w_0)$ for positive μ (i.e., negative w_0). We see that the peak of $X(w_0)$ is indeed at $-w_0 \sim 2$, i.e., $T \sim \mu/(2k_{\rm B})$, which coincides with the numerical result shown in Fig. 5(d). We also see that the peak height of $|X(w_0)|$ is almost 1, meaning that the maximal $|S|$ within this approximation is $k_{\rm B}/e \sim 86$ μV/K. In actual numerical numerical calculation [Fig. 5(d)], the peak height is smaller than the above value and it also depends on μ, which might be because α_0 is non-negligible.

The estimation of ZT can be performed in the same way. Again neglecting α_0, we have

$$ZT = Y(w_0),\ Y(w_0) = \left[\frac{[2h_1(-w_0) - w_0h_0(-w_0)][2h_3(-w_0) - w_0h_2(-w_0)]}{[h_2(-w_0) - 2w_0h_1(-w_0)]^2} - 1\right]^{-1}, \tag{B9}$$

where

$$h_3(w) = \int_w^\infty dw'\, g_3(w') = w^2\left[3\log\left(1+e^w\right) - \frac{we^w}{e^w+1}\right] + 6w{\rm Li}_2(-e^w) - 6{\rm Li}_3(-e^w). \tag{B10}$$

Figure 10(b) shows the function $Y(w_0)$. We see that the peak of $Y(w_0)$ is $-w_0 \sim 2.5$. Thus, the peak temperature of ZT is $T \sim \mu/(2.5k_{\rm B})$, which is slightly smaller than that for S. We also see that maximum of ZT is about 0.27. This value is greater than the optimal ZT obtained in the numerical calculation, which might be again due to the effect of α_0.

Appendix C: Role of Dirac points in the Seebeck coefficient for type-II case

In this appendix, we clarify how the Dirac points contribute the Seebeck coefficient. For the type-II case, the Fermi surface extends to far way from the Dirac points [Fig. 2(g)], thus it is worth investigating the contribution from the region near the Dirac points and those from the rest separately.

To do this, we first divide the $\boldsymbol{k}$ space into two regions: one is the vicinity of the Dirac points, which we call (A), and the other is the rest of (A), which we call (B) [see Fig. 11(a)]. Then, the spectral conductivity of Eq. (8) can be divided into two contributions by restricting the summation over $\boldsymbol{k}$ to either (A) or (B). We call each contribution $\alpha_{xx}^{\rm (A)}(\epsilon)$ and $\alpha_{xx}^{\rm (B)}(\epsilon)$, respectively. In Fig. 11(b), we plot $\alpha_{xx}^{\rm (A)}(\epsilon)$ and $\alpha_{xx}^{\rm (B)}(\epsilon)$. We see that these two contributions are comparable near $\epsilon = 0$ eV. Therefore, as far as the electric conductivity is concerned, the Dirac points are not of special importance.

As for the Seebeck coefficient, by substituting $\alpha_{xx}^{\rm (A)}(\epsilon)$ and $\alpha_{xx}^{\rm (B)}(\epsilon)$ into Eq. (18), we obtain $L_{12}^{\rm (A)}$ and $L_{12}^{\rm (B)}$, respectively. Using these, we define

$$S^{\rm (A)/(B)} = \frac{1}{T}\frac{L_{12}^{\rm (A)/(B)}}{L_{11}}. \tag{C1}$$

In Fig. 11(c), we plot $S^{(A)}$, $S^{(B)}$ and S as functions of T for

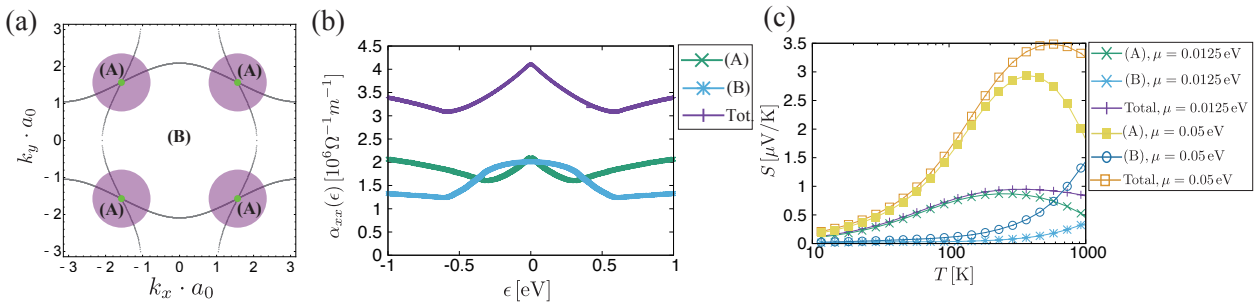

FIG. 11. (a) Schematic figure of the division of the Brillouin zone into the two regions, (A) and (B). The region (A) is composed of four circles whose radius is $\frac{\pi}{4a_0}$ and centers are the Dirac points. The gray lines are the Fermi surface for $\mu = 0$ eV. (b) $\alpha_{xx}^{(\mathrm{A})}(\epsilon)$, $\alpha_{xx}^{(\mathrm{B})}(\epsilon)$, and $\alpha_{xx}(\epsilon)$ as functions of ϵ. (c) Temperature dependence of $S^{(\mathrm{A})}$, $S^{(\mathrm{B})}$ and S. For (b) and (c), we set $\Gamma = 0.02$ eV.

$\mu = 0.0125$ eV and 0.05 eV. We see that the large contribution to S comes from the region (A) in both cases, which implies that the Dirac points play an important role in the thermoelectric transport in this system.

[1] P. R. Wallace, Phys. Rev. **71**, 622 (1947).
[2] K. S. Novoselov, A. K. Geim, S. V. Morozov, D. Jiang, Y. Zhang, S. V. Dubonos, I. V. Grigorieva, and A. A. Firsov, Science **306**, 666 (2004).
[3] A. H. Castro Neto, F. Guinea, N. M. R. Peres, K. S. Novoselov, and A. K. Geim, Rev. Mod. Phys. **81**, 109 (2009).
[4] K. Kajita, Y. Nishio, N. Tajima, Y. Suzumura, and A. Kobayashi, Journal of the Physical Society of Japan **83**, 072002 (2014).
[5] S. Katayama, A. Kobayashi, and Y. Suzumura, Journal of the Physical Society of Japan **75**, 054705 (2006).
[6] A. Kobayashi, S. Katayama, Y. Suzumura, and H. Fukuyama, Journal of the Physical Society of Japan **76**, 034711 (2007).
[7] H. Fukuyama, Journal of the Physical Society of Japan **76**, 043711 (2007).
[8] M. O. Goerbig, J.-N. Fuchs, G. Montambaux, and F. Piéchon, Phys. Rev. B **78**, 045415 (2008).
[9] A. Kobayashi, Y. Suzumura, and H. Fukuyama, Journal of the Physical Society of Japan **77**, 064718 (2008).
[10] A. Kobayashi, Y. Suzumura, H. Fukuyama, and M. O. Goerbig, Journal of the Physical Society of Japan **78**, 114711 (2009).
[11] G. E. Volovik, JETP Letters **104**, 645 (2016).
[12] G. E. Volovik and K. Zhang, Journal of Low Temperature Physics **189**, 276 (2017).
[13] G. E. Volovik, Physics-Uspekhi **61**, 89 (2018).
[14] H. Liu, J.-T. Sun, C. Cheng, F. Liu, and S. Meng, Phys. Rev. Lett. **120**, 237403 (2018).
[15] H. Huang, K.-H. Jin, and F. Liu, Phys. Rev. B **98**, 121110 (2018).
[16] S. Fragkos, R. Sant, C. Alvarez, E. Golias, J. Marquez-Velasco, P. Tsipas, D. Tsoutsou, S. Aminalragia-Giamini, E. Xenogiannopoulou, H. Okuno, G. Renaud, O. Rader, and A. Dimoulas, Phys. Rev. Materials **3**, 104201 (2019).
[17] M. Milićević, G. Montambaux, T. Ozawa, O. Jamadi, B. Real, I. Sagnes, A. Lemaître, L. Le Gratiet, A. Harouri, J. Bloch, and A. Amo, Phys. Rev. X **9**, 031010 (2019).
[18] T. Farajollahpour, Z. Faraei, and S. A. Jafari, Phys. Rev. B **99**, 235150 (2019).
[19] J. Kim, S. Yu, and N. Park, Phys. Rev. Applied **13**, 044015 (2020).
[20] Y.-G. Chen, X. Luo, F.-Y. Li, B. Chen, and Y. Yu, Phys. Rev. B **101**, 035130 (2020).
[21] L. Jin, H. C. Wu, B.-B. Wei, and Z. Song, Phys. Rev. B **101**, 045130 (2020).
[22] Z. Gong, X. Shi, J. Li, S. Li, C. He, T. Ouyang, C. Zhang, C. Tang, and J. Zhong, Phys. Rev. B **101**, 155427 (2020).
[23] L. Jin, X. Zhang, Y. Liu, X. Dai, L. Wang, and G. Liu, Phys. Rev. B **102**, 195104 (2020).
[24] T. Farajollahpour and S. A. Jafari, Phys. Rev. Research **2**, 023410 (2020).
[25] S. Fragkos, P. Tsipas, E. Xenogiannopoulou, Y. Panayiotatos, and A. Dimoulas, Journal of Applied Physics **129**, 075104 (2021).
[26] X.-P. Li, K. Deng, B. Fu, Y. Li, D.-S. Ma, J. Han, J. Zhou, S. Zhou, and Y. Yao, Phys. Rev. B **103**, L081402 (2021).
[27] C. Sims, Condensed Matter **6**, 18 (2021).
[28] Y. Suzumura, I. Proskurin, and M. Ogata, Journal of the Physical Society of Japan **83**, 023701 (2014).
[29] Y. Suzumura, I. Proskurin, and M. Ogata, Journal of the Physical Society of Japan **83**, 094705 (2014).
[30] I. Proskurin, M. Ogata, and Y. Suzumura, Phys. Rev. B **91**, 195413 (2015).
[31] A. Mani and C. Benjamin, Phys. Rev. E **96**, 032118 (2017).
[32] A. Mani and C. Benjamin, The Journal of Physical Chemistry C **123**, 22858 (2019).
[33] A. Mani, S. Pal, and C. Benjamin, Scientific Reports **9**, 6018 (2019).
[34] M. Koshino and T. Ando, Phys. Rev. B **76**, 085425 (2007).
[35] M. Koshino and T. Ando, Phys. Rev. B **81**, 195431 (2010).
[36] G. Gómez-Santos and T. Stauber, Phys. Rev. Lett. **106**, 045504 (2011).
[37] A. Raoux, F. Piéchon, J.-N. Fuchs, and G. Montambaux, Phys. Rev. B **91**, 085120 (2015).
[38] M. Ogata, Journal of the Physical Society of Japan **85**, 104708 (2016).
[39] Y. Ferreiros, A. A. Zyuzin, and J. H. Bardarson, Phys. Rev. B **96**, 115202 (2017).
[40] V. Kozii, B. Skinner, and L. Fu, Phys. Rev. B **99**, 155123 (2019).
[41] S. Rostamzadeh, i. d. I. m. c. Adagideli, and M. O. Goerbig, Phys. Rev. B **100**, 075438 (2019).

[42] A. Mawrie and B. Muralidharan, Phys. Rev. B **100**, 081403 (2019).
[43] I. Mandal and K. Saha, Phys. Rev. B **101**, 045101 (2020).
[44] D. Ohki, Y. Omori, and A. Kobayashi, Phys. Rev. B **101**, 245201 (2020).
[45] T. M. McCormick, I. Kimchi, and N. Trivedi, Phys. Rev. B **95**, 075133 (2017).
[46] T. M. McCormick, R. C. McKay, and N. Trivedi, Phys. Rev. B **96**, 235116 (2017).
[47] R. C. McKay, T. M. McCormick, and N. Trivedi, Phys. Rev. B **99**, 245119 (2019).
[48] T. Mizoguchi and Y. Hatsugai, Journal of the Physical Society of Japan **89**, 103704 (2020).
[49] R. Kubo, Journal of the Physical Society of Japan **12**, 570 (1957).
[50] J. M. Luttinger, Phys. Rev. **135**, A1505 (1964).
[51] E. H. Hwang, S. Adam, and S. D. Sarma, Phys. Rev. Lett. **98**, 186806 (2007).
[52] E. H. Hwang, E. Rossi, and S. Das Sarma, Phys. Rev. B **80**, 235415 (2009).
[53] G. D. Mahan, Many-Particle Physics (Plenum, New York, 1990).
[54] T. Yamamoto and H. Fukuyama, Journal of the Physical Society of Japan **87**, 024707 (2018).
[55] M. Ogata and H. Fukuyama, Journal of the Physical Society of Japan **88**, 074703 (2019).
[56] S. K. Jacimovski, M. Bukurov, J. P. Setrajcic, and D. I. RakoviC, Superlattices and Microstructures **88**, 330 (2015).
[57] M. Jonson and G. D. Mahan, Phys. Rev. B **21**, 4223 (1980).
[58] H. Kontani, Phys. Rev. B **67**, 014408 (2003).
[59] A. Sommerfeld and H. Bethe, Elektronentheorie der Metalle, Handbuch der Physik, Vol. 24/2 (Springer, Berlin/Heidelberg, 1933).
[60] H. Matsuura, H. Maebashi, M. Ogata, and H. Fukuyama, Journal of the Physical Society of Japan **88**, 074601 (2019).
[61] N. F. Mott and H. Jones, The Theory of the Properties of Metals and Alloys (Dover New York, 1936).
[62] M. Inokuchi, H. Tajima, A. Kobayashi, T. Ohta, H. Kuroda, R. Kato, T. Naito, and H. Kobayashi, Bulletin of the Chemical Society of Japan **68**, 547 (1995).
[63] T. Tsumuraya and Y. Suzumura, Eur. Phys. J. B **94**, 17 (2021).
[64] S. Kitou, T. Tsumuraya, H. Sawahata, F. Ishii, K.-i. Hiraki, T. Nakamura, N. Katayama, and H. Sawa, Phys. Rev. B **103**, 035135 (2021).
[65] T. Konoike, M. Sato, K. Uchida, and T. Osada, Journal of the Physical Society of Japan **82**, 073601 (2013).
[66] R. Kitamura, N. Tajima, K. Kajita, R. Kato, M. Tamura, T. Naito, and Y. Nishio, Proceedings of the 12th Asia Pacific Physics Conference (APPC12) **1**, 012097.
[67] A. Kobayashi, S. Katayama, K. Noguchi, and Y. Suzumura, Journal of the Physical Society of Japan **73**, 3135 (2004).
[68] K. Kishigi and Y. Hasegawa, Phys. Rev. B **96**, 085430 (2017).
[69] G. D. Mahan and J. O. Sofo, Proceedings of the National Academy of Sciences **93**, 7436 (1996).
[70] E. H. Hasdeo, L. P. A. Krisna, M. Y. Hanna, B. E. Gunara, N. T. Hung, and A. R. T. Nugraha, Journal of Applied Physics **126**, 035109 (2019).